

# Chen's derivative rule revisited: Role of tip-orbital interference in STM

Gábor Mándi and Krisztián Palotás

*Department of Theoretical Physics, Budapest University of Technology and Economics,  
Budafoki út 8., H-1111 Budapest, Hungary*

## Abstract

On the occasion of its 25th anniversary, we revise Chen's derivative rule for electron tunneling [C. J. Chen, Phys. Rev. B 42, 8841 (1990)] for the purpose of computationally efficient simulations of scanning tunneling microscopy (STM) based on first principles electronic structure data. The revised model allows the weighting of tunneling matrix elements of different tip orbital characters by an arbitrary energy independent choice or based on energy dependent weighting coefficients obtained by an expansion of the tip single electron wavefunctions/density of states projected onto the tip apex atom. Tip-orbital interference in the STM junction is included in the model by construction and can be analyzed quantitatively. As a further advantage, arbitrary tip geometrical orientations are included in the revised model by rotating the coordinate system of the tip apex using Euler angles and redefining the weighting coefficients of the tunneling matrix elements. We demonstrate the reliability of the model by applying it to two functionalized surfaces of recent interest where quantum interference effects play an important role in the STM imaging process: N-doped graphene and a magnetic  $\text{Mn}_2\text{H}$  complex on the Ag(111) surface. We find that the proposed tunneling model is 25 times faster than the Bardeen method concerning computational time, while maintaining good agreement. Our results show that the electronic structure of the tip has a considerable effect on STM images, and the Tersoff-Hamann model does not always provide sufficient results in view of quantum interference effects. For both studied surfaces we highlight the importance of interference between  $s$  and  $p_z$  tip orbitals that can cause a significant contrast change in the STM images. Our method, thus, provides a fast and reliable tool for calculating STM images based on Chen's derivative rule taking into account the electronic structure and local geometry of the tip apex.

PACS numbers: 68.37.Ef, 71.15.-m, 73.63.-b

## I. INTRODUCTION

The role of the tip in scanning tunneling microscopy (STM) on the imaging contrast mechanisms has been extensively studied in recent years. A reliable interpretation of experimental findings can be obtained by STM simulations that need electron tunneling models capable of dealing with a diversity of tip parameters in a consistent manner. Furthermore, it is required that STM simulations are computationally inexpensive and user-friendly in order to provide a useful tool not only for theoretician experts of electronic structure methods but also for experimental STM groups.

The pioneering electron tunneling model was proposed by Bardeen who derived the tunneling current formula based on first order perturbation theory [1]. While this method contains the effect of the electronic structure of the STM tip explicitly, it is only applicable in the pure tunneling regime and does not account for multiple scattering effects. An extension of the Bardeen method including multiple scattering has been proposed by Palotás and Hofer [2] that has been implemented in the BSKAN code [3]. Using the Keldysh nonequilibrium Green's function formalism, Mingo *et al.* developed an electron transport model that is valid in both tunneling and close-contact regimes [4]. These methods require the single electron wavefunctions or Green's functions of the sample surface and the tip or of the coupled system that can be obtained from first principles electronic structure calculations. Although these single electron quantities can routinely be calculated, e.g., by using density functional theory (DFT), STM image simulations are still considered as computationally demanding if performed at high levels of electron transport theory. The reason is the numerous parameters affecting the electron tunneling that have to be considered if aiming at an accurate interpretation of STM experiments, e.g., the bias voltage, the tunneling current or tip-sample distance and the tip characteristics: material, geometry, functionalization, termination, orientation, and the corresponding electronic structure. Note that the modeling of the tip needs special effort as the above listed tip parameters can be chosen in practically infinite combinations.

To overcome the computational drawback of high level electron transport theories, several simplifications have been introduced. Tersoff and Hamann assumed an *s*-wave tip [5, 6]. This way the Bardeen current formula has been recast to contain the electronic structure of the sample surface only. In the Tersoff-Hamann model the tunneling current is proportional to

the integrated local density of states of the sample at the position of the tip. The energy integral corresponds to the bias voltage. This approach has become the most widely used method for simulating STM and scanning tunneling spectroscopy (STS) due to its relative simplicity, although it completely neglects the effects of the STM tip.

Allowing more generality for the tip orbitals, Chen derived the so-called derivative rule from the Bardeen current formula, where the resulting tunneling matrix element is proportional to the linear combination of spatial derivatives of single electron wavefunctions of the sample surface in the vacuum [7]. The spatial derivatives are determined by the orbital characters of the STM tip. However, practical calculations of the coefficients for the linear combination were not reported. The determination of the energy dependent coefficients in Chen’s derivative rule from first principles calculations is one of the subjects of the present work. Palotás *et al.* developed a tunneling model using the three-dimensional Wentzel-Kramers-Brillouin (3D-WKB) theory [8] that accounts for the energy dependent combination of tip orbital characters determined from the orbitally decomposed DOS projected to the tip apex atom [9]. We will show that the orbital-decomposed projected tip DOS can be related to an approximation of the tunneling matrix weighting coefficients in the revised Chen’s derivative rule.

The above mentioned tunneling models have been successfully used in theoretical investigations of a multitude of STM junctions. To select a few examples, we focus on studies concerned with the role of the tip geometry, orbital character and functionalization on the STM imaging. Teobaldi *et al.* investigated the effect of bias voltage and tip electronic structure on the STM contrast formation of the highly oriented pyrolytic graphite (HOPG) surface using tungsten tips with different terminations and sharpnesses [10]. Chaika *et al.* demonstrated that by using oriented single crystalline tungsten tips it is possible to select a particular tip electron orbital for high-resolution imaging of HOPG [11, 12]. Channel selective tunneling was also examined by Wong *et al.* using tip functionalization with hexa-peri-hexabenzocoronene (HBC) molecules [13]. Employing Chen’s derivative rule, Gross *et al.* simulated STM images of pentacene and naphthalocyanine molecules using CO-functionalized tips [14]. The increased lateral resolution achieved by these tips demonstrated the significant contribution of  $p$ -type tip states. Siegert *et al.* studied the influence of  $s$ - and  $p$ -wave tip symmetries on the STM maps of  $\pi$ -conjugated molecules using the reduced density matrix

formalism combined with Chen’s derivative rule [15]. The orbital-dependent 3D-WKB model was extended for spin-polarized STM in Ref. [16]. The effect of tip orbital symmetries on the scanning tunneling spectra was also investigated by probing the cuprate high-temperature superconductor  $\text{Bi}_2\text{Sr}_2\text{CaCu}_2\text{O}_{8+\delta}$ . Suominen *et al.* found that the symmetry of the tip can radically change the topographic image due to the overlap of sample and tip orbitals [17], while da Silva Neto *et al.* stated that the apparent nematic behavior of the lattice is likely related to a realistic STM tip probing the band structure of the material [18]. They also pointed out the importance of tunneling interference effects in the STM junction.

The effect of inter- and intra-atomic interference of electron orbitals has also been in the focus of several studies. Telychko *et al.* investigated the nitrogen-doped graphene surface with tungsten and diamond tips and found significantly smaller current (dip) above the nitrogen atom than above the neighboring carbon atoms at constant height [19]. This finding has been explained by a destructive quantum interference essentially resulting from the C-N  $\pi$ -bond. Using the Keldysh Green’s function formalism, Jurczyszyn and Stankiewicz and Mingo *et al.* extensively investigated inter-orbital interference effects in various tip-sample combinations and found that the interference has a considerable influence on STM images and STS spectra [4, 20, 21]. Sachse *et al.* showed that an antiferromagnetic alignment of Mn spin moments in a  $\text{Mn}_2\text{H}$  complex on the Ag(111) surface explains the experimental STM observation of a dip above the middle of the Mn dimer [22]. In the present work we point out that a destructive quantum interference between  $s$  and  $p_z$  tip orbitals contributes to the emergence of such a dip in the STM image.

Very recently, the role of the spatial orientation of the tip in the tunneling process has been the subject of a few studies. Hagelaar *et al.* performed STM simulations of NO adsorbed on Rh(111) surface over a wide range of tip apex terminations and orientations and compared them with experimental STM images [23]. They found that asymmetric tip orientations provide good qualitative agreement with the experiments under certain tunneling conditions. Lakin *et al.* developed a technique to recover the relative orientation of a  $\text{C}_{60}$ -functionalized tip and a  $\text{C}_{60}$  molecule adsorbed on the Si(111)-(7 $\times$ 7) surface based on Chen’s derivative rule [24]. Using the 3D-WKB method, Mándi *et al.* studied tip rotational effects on the imaging of HOPG(0001) [25] and W(110) surfaces [26] and found that the STM images can considerably be distorted due to different spatial orientations of the tip. Although the 3D-

WKB method lacks the inclusion of electron interference, it proved to be useful for statistically determining the geometry and likely orientations of the tip in bias voltage dependent STM experiments of HOPG based on previously inaccessible large scale simulations of tip models in a computationally efficient way [27]. The conclusion of all these listed studies is that the relative orientation of the sample surface and the local tip apex geometry is far from being highly symmetric that is usually considered in standard STM simulations nowadays. Therefore, it is clear that spatial orientations of the tip have to be integrated into STM simulation models, thus, the second subject of the present work is to include arbitrary tip geometrical orientations into Chen's derivative rule.

The paper is organized as follows. The revised Chen's derivative rule is presented in section II. Computational details of the electronic structure calculations of surface and tip models are reported in section III. Results of simulated STM images and comparisons with other electron tunneling methods are found in section IV A and IV B for the N-doped graphene and for the antiferromagnetic Mn<sub>2</sub>H complex on Ag(111) surface, respectively. We summarize our findings in section V.

## II. REVISED CHEN'S DERIVATIVE RULE

In the tunneling regime the current  $I$  depending on the bias voltage  $V$  between the sample surface and the tip can be calculated using Bardeen's tunneling formula [1],

$$I(V) = \frac{2\pi e}{\hbar} \sum_{\mu\nu} f(E_\mu) [1 - f(E_\nu + eV)] |M_{\mu\nu}|^2 \delta(E_\mu - E_\nu - eV), \quad (1)$$

where  $e$  is the elementary charge,  $\hbar$  is the reduced Planck constant,  $f$  is the Fermi distribution function and  $M_{\mu\nu}$  is the tunneling matrix element between two single electron states of the sample ( $\mu$ ) and the tip ( $\nu$ ) involved in the tunneling.  $E_\mu$  and  $E_\nu$  denote corresponding Kohn-Sham eigenenergies that can be obtained from first principles calculations. Note that  $\mu$  and  $\nu$  denote composite indices of the band ( $n$ ), wave vector ( $\mathbf{k}_\parallel$ ) and spin ( $\sigma$ ) in the separate sample and tip subsystems, respectively. The tunneling matrix element can be calculated as an integral over the  $\mathcal{S}$  separation surface in the vacuum between the sample and the tip,

$$M_{\mu\nu} = -\frac{\hbar^2}{2m} \int_{\mathcal{S}} (\chi_\nu^* \nabla \psi_\mu - \psi_\mu \nabla \chi_\nu^*) \mathbf{dS}. \quad (2)$$

In the model the tunneling is assumed to be elastic and energy conservation is ensured by the Dirac-delta in Eq. (1). At finite temperature the thermal broadening of the electron states has to be taken into account. This is usually done by approximating the Dirac-delta with a Gaussian function,

$$\delta(E_\mu - E_\nu - eV) \sim \frac{1}{\sqrt{2\pi}\Delta^2} \exp\left[-\frac{(E_\mu - E_\nu - eV)^2}{2\Delta^2}\right]. \quad (3)$$

In principle, all  $\mu - \nu$  transitions have to be considered with the probability given by this Gaussian factor (and  $|M_{\mu\nu}|^2$ ) when calculating the tunneling current but practically transitions with significantly low probability can be neglected, e.g., if  $|E_\mu - E_\nu - eV| \geq 3\Delta$ , where  $\Delta = k_B T$  is the thermal broadening of the states at  $T$  temperature with  $k_B$  the Boltzmann constant.

Chen's approach is based on the expansion of the tip wavefunction into spherical harmonic components around the tip apex position  $\mathbf{r}_0$  [7],

$$\chi_\nu(\mathbf{r}) = \sum_{lm} C_{\nu lm} k_l(\kappa_\nu r) Y_{lm}(\vartheta, \varphi), \quad (4)$$

where  $r = |\mathbf{r} - \mathbf{r}_0|$ ,  $k_l$  is the spherical modified Bessel function of the second kind,  $Y_{lm}$  is the spherical harmonic function depending on the azimuthal ( $\vartheta$ ) and polar ( $\varphi$ ) angles and  $\kappa_\nu$  is the vacuum decay of the tip wavefunction. The expansion can also be performed according to the real space orbital characters  $\beta \in \{s, p_y, p_z, p_x, d_{xy}, d_{yz}, d_{3z^2-r^2}, d_{xz}, d_{x^2-y^2}\}$  introducing the notation of  $\tilde{Y}_{\nu\beta}(r, \vartheta, \varphi) = k_\beta(\kappa_\nu r) Y_\beta(\vartheta, \varphi)$  with  $Y_\beta$  real spherical harmonics as

$$\chi_\nu(\mathbf{r}) = \sum_{\beta} C_{\nu\beta} \tilde{Y}_{\nu\beta}(r, \vartheta, \varphi). \quad (5)$$

Using this expansion of the tip wavefunction in Eq. (2) leads to Chen's derivative rule, and  $|M_{\mu\nu}|^2$  can be written as

$$|M_{\mu\nu}|^2 = \frac{4\pi^2 \hbar^4}{\kappa_\nu^2 m^2} \left| \sum_{\beta} C_{\nu\beta} \hat{\partial}_{\nu\beta} \psi_\mu(\mathbf{r}_0) \right|^2. \quad (6)$$

We introduce a new notation,  $M_{\mu\nu\beta} = C_{\nu\beta} \hat{\partial}_{\nu\beta} \psi_\mu(\mathbf{r}_0)$  that corresponds to the tunneling matrix element of a given orbital symmetry ( $\beta$ ). Here, the differential operator  $\hat{\partial}_{\nu\beta}$  acts on the sample wavefunction at the tip apex position  $\mathbf{r}_0$ . Note that  $\hat{\partial}_{\nu\beta}$  is dimensionless as it contains a factor

$\beta$	$s$	$p_y$	$p_z$	$p_x$	$d_{xy}$	$d_{yz}$	$d_{3z^2-r^2}$	$d_{xz}$	$d_{x^2-y^2}$
$\hat{\partial}_{\nu\beta}$	1	$\frac{1}{\kappa_\nu} \frac{\partial}{\partial y}$	$\frac{1}{\kappa_\nu} \frac{\partial}{\partial z}$	$\frac{1}{\kappa_\nu} \frac{\partial}{\partial x}$	$\frac{1}{\kappa_\nu^2} \frac{\partial^2}{\partial x \partial y}$	$\frac{1}{\kappa_\nu^2} \frac{\partial^2}{\partial y \partial z}$	$\frac{3}{\kappa_\nu^2} \frac{\partial^2}{\partial z^2} - 1$	$\frac{1}{\kappa_\nu^2} \frac{\partial^2}{\partial x \partial z}$	$\frac{1}{\kappa_\nu^2} (\frac{\partial^2}{\partial x^2} - \frac{\partial^2}{\partial y^2})$

Table I. Differential operators  $\hat{\partial}_{\nu\beta}$  for given orbital symmetries ( $\beta$ ) according to Chen [7].

$\kappa_\nu^{-l}$  with  $l$  being the angular quantum number. The differential operators for the given orbital characters are summarized in Table I following Chen [7].

Rewriting Eq. (6) as

$$|M_{\mu\nu}|^2 = \frac{4\pi^2\hbar^4}{\kappa_\nu^2 m^2} \sum_{\beta} \sum_{\beta'} M_{\mu\nu\beta}^* M_{\mu\nu\beta'} = \frac{4\pi^2\hbar^4}{\kappa_\nu^2 m^2} \left[ \sum_{\beta} |M_{\mu\nu\beta}|^2 + \sum_{\beta \neq \beta'} 2\text{Re}\{M_{\mu\nu\beta}^* M_{\mu\nu\beta'}\} \right] \quad (7)$$

allows the investigation of different contributions to the tunneling current. The first term of the equation on the right hand side is the sum of the absolute value squares of  $M_{\mu\nu\beta} = C_{\nu\beta} \hat{\partial}_{\nu\beta} \psi_\mu(\mathbf{r}_0)$ , which is always positive, hence this term provides a positive contribution to the tunneling current. The second term is an interference term concerning tip orbitals, which is real and the sign of the individual  $\beta \neq \beta'$  components can be positive or negative, respectively contributing as constructive or destructive interference to the tunneling current. The analysis of the ratios and polarities of the listed components of  $|M_{\mu\nu}|^2$  gives the opportunity to obtain a deeper physical understanding of the electron tunneling process. Note that in Eq. (6) the sample wavefunction  $\psi_\mu$  can also be expanded into spherical harmonics similarly to Eq. (5). This way the interference of the sample orbitals and interference between sample and tip orbitals can be investigated as well. A similar decomposition of tunneling matrix elements has been used by Jurczyszyn and Stankiewicz [20, 21] and Mingo *et al.* [4].

### A. Calculation of spatial derivatives

The spatial derivatives (see Table I) of the sample wavefunction for  $M_{\mu\nu\beta} = C_{\nu\beta} \hat{\partial}_{\nu\beta} \psi_\mu(\mathbf{r}_0)$  can be calculated straightforwardly when using a plane wave expansion of the wavefunctions. There are many DFT codes, which use a plane wave basis set, e.g., VASP [28], ABINIT [29] and Quantum-Espresso [30] to name a few popular ones. Thus, the presented forms of the spatial derivatives can be potentially useful for future implementations of the revised Chen's derivative rule. In the present work we use wavefunctions obtained from the VASP code. Let us assume that the single electron wavefunctions of the sample surface are given in the

vacuum at position vector  $\mathbf{r}$  in a two-dimensional (2D) Fourier-grid as

$$\psi_\mu(\mathbf{r}) = \psi_{n^S \mathbf{k}_\parallel^S \sigma^S}(\mathbf{r}) = \sum_{\mathbf{G}_\parallel} A_{n^S \mathbf{k}_\parallel^S \sigma^S}(\mathbf{G}_\parallel, z) \exp [i(\mathbf{k}_\parallel^S + \mathbf{G}_\parallel)\mathbf{r}_\parallel], \quad (8)$$

where  $\mu = (n^S \mathbf{k}_\parallel^S \sigma^S)$  is the composite index for single electron states of the sample with  $\mathbf{k}_\parallel^S = (k_x^S, k_y^S)$  the lateral component of the wave vector. The derivation with respect to  $z$  (the direction perpendicular to the sample surface) acts on the expansion coefficients only,

$$\frac{\partial}{\partial z} \psi_{n^S \mathbf{k}_\parallel^S \sigma^S}(\mathbf{r}) = \sum_{\mathbf{G}_\parallel} \left( \frac{\partial}{\partial z} A_{n^S \mathbf{k}_\parallel^S \sigma^S}(\mathbf{G}_\parallel, z) \right) \exp [i(\mathbf{k}_\parallel^S + \mathbf{G}_\parallel)\mathbf{r}_\parallel], \quad (9)$$

while the  $x$ - and  $y$ -derivatives act on the phase factor,

$$\frac{\partial}{\partial x} \psi_{n^S \mathbf{k}_\parallel^S \sigma^S}(\mathbf{r}) = \sum_{\mathbf{G}_\parallel} i(k_x^S + G_x) A_{n^S \mathbf{k}_\parallel^S \sigma^S}(\mathbf{G}_\parallel, z) \exp [i(\mathbf{k}_\parallel^S + \mathbf{G}_\parallel)\mathbf{r}_\parallel], \quad (10)$$

$$\frac{\partial}{\partial y} \psi_{n^S \mathbf{k}_\parallel^S \sigma^S}(\mathbf{r}) = \sum_{\mathbf{G}_\parallel} i(k_y^S + G_y) A_{n^S \mathbf{k}_\parallel^S \sigma^S}(\mathbf{G}_\parallel, z) \exp [i(\mathbf{k}_\parallel^S + \mathbf{G}_\parallel)\mathbf{r}_\parallel]. \quad (11)$$

The same procedure can be applied for higher order derivatives listed in Table I.

## B. Determination of weighting coefficients

We report on three ways for the choice of the weighting coefficients  $C_{\nu\beta}$  for  $M_{\mu\nu\beta} = C_{\nu\beta} \hat{\partial}_{\nu\beta} \psi_\mu(\mathbf{r}_0)$ .

(i) The simplest choice is the assumption of an idealized tip with a given set of energy independent weighting factors  $\{C_\beta\}$ . Such examples can be found in the literature. In the study of Gross *et al.* a CO-functionalized tip was modeled as a combination of  $s$  and  $p$  orbitals and interference terms were neglected [14]. Siegert *et al.* employed the reduced density matrix formalism combined with Chen's derivative rule with the inclusion of interference effects and they considered a similar combination of  $s$  and  $p$  orbitals [15]. Generally,  $C_\beta$  can be a complex number. We restrict the choice of the set of  $\{C_\beta\}$  to fulfill the condition:  $\sum_\beta |C_\beta|^2 = 1$ . Moreover, in this idealized tip model case we choose the vacuum decay of the tip states  $\kappa_\nu = 1 \text{ \AA}^{-1}$  for all  $\nu$ . Examples of the effect of idealized tips as pure  $s$  and pure  $p_z$  orbitals and a combination of  $(s + p_z)/\sqrt{2}$  on the STM image of N-doped graphene will be shown in section IV A. We will also point out that the effect of interference is remarkable in this case causing a significant contrast change.



(ii) Based on Eq. (5),  $C_{\nu\beta}$  complex numbers can be obtained as

$$C_{\nu\beta} = \left\langle \tilde{Y}_{\nu\beta}(\mathbf{r}) \middle| \chi_{\nu}(\mathbf{r}) \right\rangle = \langle k_{\beta}(\kappa_{\nu}r)Y_{\beta}(\vartheta, \varphi) | \chi_{\nu}(\mathbf{r}) \rangle \quad (12)$$

with  $\nu = (n^T \mathbf{k}_{\parallel}^T \sigma^T)$  composite index for single electron states of the tip, where  $\mathbf{k}_{\parallel}^T$  is the lateral component of the wave vector. We calculate these coefficients explicitly in the Wigner-Seitz sphere ( $W - S$ ) of the tip apex atom with the VASP code. Since symmetry properties of the model tip geometry are taken into account in VASP, we obtain a reduced set of  $C_{\nu\beta}$  corresponding to  $\mathbf{k}_{\parallel}^T$  being in the irreducible part of the Brillouin zone. We can calculate how these coefficients change under 2D transformations ( $\mathcal{T}$ ) of the tip's symmetry group in order to obtain  $C_{\nu\beta}$  in the full 2D Brillouin zone. For this, the plane wave expansion of the tip wavefunction is needed,

$$\chi_{\nu}(\mathbf{r}) = \chi_{n^T \mathbf{k}_{\parallel}^T \sigma^T}(\mathbf{r}) = \sum_{\mathbf{G}_{\parallel}} B_{n^T \mathbf{k}_{\parallel}^T \sigma^T}(\mathbf{G}_{\parallel}, z) \exp [i(\mathbf{k}_{\parallel}^T + \mathbf{G}_{\parallel})\mathbf{r}_{\parallel}], \quad (13)$$

similarly to Eq. (8). Since the  $B$  expansion coefficients are invariant under the  $\mathcal{T}$  transformation, i.e.,  $B_{n^T \mathbf{k}_{\parallel}^T \sigma^T} = B_{n^T \mathcal{T}(\mathbf{k}_{\parallel}^T) \sigma^T}$ , the transformation of the tip wavefunction comes from that of the phase factors. Using Eqs. (12) and (13) we obtain the following for the transformed coefficients,

$$\begin{aligned} C_{n^T \mathcal{T}(\mathbf{k}_{\parallel}^T) \sigma^T \beta} &= \int_{W-S} k_{\beta}(\kappa_{\nu}r)Y_{\beta}(\mathbf{r}) \sum_{\mathbf{G}_{\parallel}} B_{\nu}(\mathbf{G}_{\parallel}, z) \exp [i\mathcal{T}(\mathbf{k}_{\parallel}^T + \mathbf{G}_{\parallel})\mathbf{r}_{\parallel}] d^3r \\ &= \int_{W-S} k_{\beta}(\kappa_{\nu}r)Y_{\beta}(\mathcal{T}\mathbf{r})\chi_{\nu}(\mathbf{r}) d^3r. \end{aligned} \quad (14)$$

Note that  $\mathcal{T}$  are represented by  $2 \times 2$  real matrices and the transformation of the coordinates is  $\mathcal{T}\mathbf{r} = (\mathcal{T}_{11}x + \mathcal{T}_{12}y, \mathcal{T}_{21}x + \mathcal{T}_{22}y, z)$ . Using the real spherical harmonics in Cartesian coordinates, we can calculate their transformations by substituting the transformed lateral coordinates into their normalized form. The results are shown in Table II. Thus,  $C_{\nu\beta}$  is determined in the full 2D Brillouin zone, and we can directly apply them in the formula of the tunneling matrix elements in Eq. (6).

(iii) The third suggestion for  $C_{\nu\beta}$  is based on the orbital-decomposed DOS projected to the tip apex atom,  $n^{TIP}(E) = \sum_{\beta} n_{\beta}^{TIP}(E) = \sum_{\beta} \sum_{\nu} n_{\nu\beta}^{TIP} \delta(E - E_{\nu})$  obtained from first principles calculation. Using the expansion of the tip wavefunction in Eq. (5) and the approximation of orthonormality for  $\tilde{Y}_{\nu\beta}(r, \vartheta, \varphi)$  within the Wigner-Seitz ( $W - S$ ) sphere of

Orbital	$Y(x, y, z)$	Transformed orbital
$s$	$\frac{1}{2\sqrt{\pi}}$	$s$
$p_y$	$\frac{1}{2}\sqrt{\frac{3}{\pi}}\frac{y}{r}$	$\mathcal{T}_{21}p_x + \mathcal{T}_{22}p_y$
$p_z$	$\frac{1}{2}\sqrt{\frac{3}{\pi}}\frac{z}{r}$	$p_z$
$p_x$	$\frac{1}{2}\sqrt{\frac{3}{\pi}}\frac{x}{r}$	$\mathcal{T}_{11}p_x + \mathcal{T}_{12}p_y$
$d_{xy}$	$\frac{1}{2}\sqrt{\frac{15}{\pi}}\frac{xy}{r^2}$	$(\mathcal{T}_{11}\mathcal{T}_{22} + \mathcal{T}_{12}\mathcal{T}_{21})d_{xy} + 2\mathcal{T}_{11}\mathcal{T}_{21}d_{x^2-y^2}$
$d_{yz}$	$\frac{1}{2}\sqrt{\frac{15}{\pi}}\frac{yz}{r^2}$	$\mathcal{T}_{21}d_{xz} + \mathcal{T}_{22}d_{yz}$
$d_{3z^2-r^2}$	$\frac{1}{4}\sqrt{\frac{5}{\pi}}\frac{3z^2-r^2}{r^2}$	$d_{3z^2-r^2}$
$d_{xz}$	$\frac{1}{2}\sqrt{\frac{15}{\pi}}\frac{xz}{r^2}$	$\mathcal{T}_{11}d_{xz} + \mathcal{T}_{12}d_{yz}$
$d_{x^2-y^2}$	$\frac{1}{4}\sqrt{\frac{15}{\pi}}\frac{x^2-y^2}{r^2}$	$(\mathcal{T}_{11}^2 - \mathcal{T}_{21}^2)d_{x^2-y^2} + 2\mathcal{T}_{11}\mathcal{T}_{12}d_{xy}$

Table II. Transformation of real spherical harmonics under 2D symmetry operations ( $\mathcal{T}$ ) of the tip.

the tip apex atom,  $\langle \tilde{Y}_{\nu\beta}(r, \vartheta, \varphi) | \tilde{Y}_{\nu\beta'}(r, \vartheta, \varphi) \rangle_{W-S} \approx \delta_{\beta\beta'}$ , the following is obtained,

$$n^{TIP}(E) = \sum_{\nu} \sum_{\beta} n_{\nu\beta}^{TIP} \delta(E - E_{\nu}) = \sum_{\nu} \langle \chi_{\nu} | \chi_{\nu} \rangle_{W-S} \delta(E - E_{\nu}) \approx \sum_{\nu} \sum_{\beta} |C_{\nu\beta}|^2 \delta(E - E_{\nu}). \quad (15)$$

Thus, we can approximate the complex  $C_{\nu\beta}$  coefficients with real values,  $C_{\nu\beta} \approx \sqrt{n_{\nu\beta}^{TIP}}$ . This way Eq. (6) is recast to

$$|M_{\mu\nu}|^2 = \frac{4\pi^2 \hbar^4}{\kappa_{\nu}^2 m^2} \left| \sum_{\beta} \sqrt{n_{\nu\beta}^{TIP}} \hat{\partial}_{\nu\beta} \psi_{\mu}(\mathbf{r}_0) \right|^2. \quad (16)$$

Since the calculation of the orbital-decomposed atom-projected DOS is routinely available in DFT codes, the presented approximation applied to the tip apex atom gives a widely accessible choice for the weighting coefficients in the revised Chen's derivative rule. In section IV A we will demonstrate that the STM images obtained by the  $C_{\nu\beta} \approx \sqrt{n_{\nu\beta}^{TIP}}$  approximation provide good agreement with those calculated using the proper complex  $C_{\nu\beta}$  coefficients according to Eq. (12).

### C. Inclusion of arbitrary tip orientations

Since the electronic structures of the sample surface and the tip are generally calculated independently to allow more flexibility with their geometries, arbitrary orientations of the tip

can be included into the revised Chen's method. This can be done by redefining the spatial derivatives of the sample wavefunctions corresponding to the orbital characters in the rotated coordinate system of the tip with respect to the sample surface. This rotation is described by a coordinate transformation, which is represented by a  $3 \times 3$  matrix  $\mathcal{R}$  with elements  $\mathcal{R}_i^j$ . We use the explicit form of  $\mathcal{R}$  as in Refs. [26, 27],

$$\mathcal{R} = \begin{bmatrix} \cos \varphi_0 \cos \psi_0 - \sin \varphi_0 \sin \psi_0 \cos \vartheta_0 & \cos \varphi_0 \sin \psi_0 + \sin \varphi_0 \cos \psi_0 \cos \vartheta_0 & \sin \varphi_0 \sin \vartheta_0 \\ -\sin \varphi_0 \cos \psi_0 - \cos \varphi_0 \sin \psi_0 \cos \vartheta_0 & -\sin \varphi_0 \sin \psi_0 + \cos \varphi_0 \cos \psi_0 \cos \vartheta_0 & \cos \varphi_0 \sin \vartheta_0 \\ \sin \psi_0 \sin \vartheta_0 & -\cos \psi_0 \sin \vartheta_0 & \cos \vartheta_0 \end{bmatrix} \quad (17)$$

with the Euler angles  $(\vartheta_0, \varphi_0, \psi_0)$ . Using the Einstein summation convention, the relationship between the two set of coordinates, the rotated tip coordinates  $x'^j \in \{x', y', z'\}$  and the sample coordinates  $x^i \in \{x, y, z\}$ , is the following:

$$x'^j = \frac{\partial x'^j}{\partial x^i} x^i = \mathcal{R}_i^j x^i; \quad x^i = \frac{\partial x^i}{\partial x'^j} x'^j = (\mathcal{R}^{-1})_j^i x'^j. \quad (18)$$

With the help of these, we can relate the derivatives of the sample wavefunction  $\psi$  with respect to the rotated tip coordinates  $x'^j$  to the derivatives with respect to the sample coordinates  $x^i$  as

$$\frac{\partial \psi}{\partial x'^j} = \frac{\partial \psi}{\partial x^i} \frac{\partial x^i}{\partial x'^j} = \frac{\partial \psi}{\partial x^i} (\mathcal{R}^{-1})_j^i. \quad (19)$$

Similarly, the second derivatives are

$$\frac{\partial^2 \psi}{\partial x'^k \partial x'^j} = \left( \frac{\partial^2 \psi}{\partial x^l \partial x^i} \right) (\mathcal{R}^{-1})_j^i (\mathcal{R}^{-1})_k^l. \quad (20)$$

Using Eqs. (19) and (20) the transformed  $\hat{\partial}'_{\nu\beta}$  differential operators corresponding to the rotated tip coordinate system can be constructed and employed in Eq. (6) for the tunneling matrix elements. Since the transformation is linear, this, in turn, results in redefined  $C_{\nu\beta}$  weighting coefficients in Eq. (6) for the  $\hat{\partial}'_{\nu\beta}$  operators given in the coordinate system of the sample listed in Table I.

### III. COMPUTATIONAL DETAILS

Using the revised Chen's derivative rule implemented in the BSKAN code [2, 3], STM imaging of two functionalized surfaces of current interest is investigated: N-doped graphene

and an antiferromagnetic  $\text{Mn}_2\text{H}$  complex on the  $\text{Ag}(111)$  surface in combination with several tip models. Geometrical relaxations and electronic structure calculations of the surface and tip models were performed separately using the VASP code [28] employing the projector augmented wave (PAW) method [31].

N-doped graphene is modeled as a free-standing single-layer graphene sheet in a  $7 \times 7$  surface unit cell following Ref. [19] and 16 Å-wide vacuum perpendicular to the surface to avoid unphysical interactions between neighboring slabs. One carbon atom is replaced by nitrogen in the given supercell. The generalized gradient approximation (GGA) and the exchange-correlation (XC) functional parametrized by Perdew and Wang (PW91) [32] were used together with a plane wave basis set energy cut-off of 400 eV and an  $11 \times 11 \times 1$  Monkhorst-Pack [33] k-point sampling of the Brillouin zone. We found a planar lattice structure after geometrical relaxation following N-doping, in agreement with Ref. [19].

For the revised Chen’s derivative rule, idealized model tips of pure  $s$ , pure  $p_z$  and a combination of  $(s + p_z)/\sqrt{2}$  orbitals are initially considered, see section II B (i) for details. Since N-doped graphene has been experimentally probed with tungsten tips [19], we consider three tungsten tip models with different sharpnesses and compositions:  $W_{\text{blunt}}$ ,  $W_{\text{sharp}}$  and  $W_{\text{C-apex}}$ . The  $W_{\text{blunt}}$  tip model is represented by an adatom adsorbed on the hollow site of the  $W(110)$  surface, the  $W_{\text{sharp}}$  tip is modeled as a pyramid of three-atoms height on the  $W(110)$  surface, and the  $W_{\text{C-apex}}$  tip is a sharp tungsten tip with a carbon apex atom accounting for a likely carbon contamination from the sample. More details on the used tip geometries can be found in Ref. [10].

Geometrical relaxations, search for the magnetic ground state and electronic structure calculations of an Mn monomer, Mn dimer and  $\text{Mn}_2\text{H}$  on the  $\text{Ag}(111)$  surface have been reported in Ref. [22], and an antiferromagnetic ground state for the  $\text{Mn}_2\text{H}/\text{Ag}(111)$  system has been found. We use their electronic structure results in the present paper, for more details on the modeled geometries and DFT calculations please refer to Ref. [22]. In their STM experiments silver tips have been used. Therefore, we consider blunt tips as an adatom adsorbed on the hollow site of the silver surface in two different orientations:  $\text{Ag}(001)$  and  $\text{Ag}(111)$ , in a  $3 \times 3$  surface unit cell and at least 15 Å-wide vacuum perpendicular to the surface to avoid unphysical interactions due to the slab geometry. GGA and XC functional parametrized by Perdew, Burke and Ernzerhof (PBE) [34] are employed. Moreover, a plane

wave basis set energy cut-off of 250 eV and an  $11 \times 11 \times 1$  Monkhorst-Pack [33] k-point grid centered on the  $\Gamma$  point are used. The convergence criterion for the forces acting on relaxed atoms (adatom and first full layer) is  $0.01 \text{ eV}\text{\AA}^{-1}$ .

#### IV. RESULTS AND DISCUSSION

We demonstrate the reliability of the revised Chen’s derivative rule for the mentioned N-doped graphene and antiferromagnetic  $\text{Mn}_2\text{H}$  complex on the Ag(111) surface, where quantum interference effects play an important role in the STM imaging process. This demonstration is done by qualitative and quantitative comparisons of simulated STM images with corresponding results obtained by Tersoff-Hamann and Bardeen tunneling methods. Quantitative comparison is facilitated by calculating Pearson product-moment correlation coefficients between the STM datasets [25, 27]. Importantly, we find that the revised Chen’s model is 25 times faster than the Bardeen method concerning computational time taking the same tunneling channels, while maintaining good agreement. The effects of electronic structure, orbital interference and spatial orientation of the tip on the STM images are highlighted. Since the detailed analysis of quantum interference effects and arbitrary tip orientations in STM junctions are presently highly demanding and enormously time-consuming using the Bardeen method, the implementation of the revised Chen’s derivative rule in the BSKAN code [2, 3] is a very promising tool for more efficient STM simulations providing a deeper understanding of a wide variety of physical phenomena in STM junctions, e.g., quantum interference and tip geometry effects.

##### A. N-doped graphene

Experimental studies have shown that in the constant height STM images of N-doped graphene the tunneling current above the N atom is significantly lower than above the neighboring C atoms [19]. At first sight this seems to be in contradiction with the fact that the density of states of the N atom is larger than that of the neighboring C atoms close to the Fermi level. The current dip above the N atom has been explained by a destructive interference between the orbitals of the N and the nearest neighbor C atoms, a pure sample effect [19]. Such a quantum interference effect is an ideal candidate to study with the revised

Chen’s method.

We have calculated constant height STM images of the N-doped graphene surface using four different tunneling models: 3D-WKB, Tersoff-Hamann, revised Chen and Bardeen. The constant height STM simulations were performed at relatively small tip-sample distance (4 Å) at two selected bias voltages ( $\pm 0.4$  V) corresponding to the STM experiments by Telychko *et al.* [19]. First, the 3D-WKB method [8] has been used. This model takes into account the orbital characteristics and electronic structure of the sample and the tip as well, but uses the atom-projected density of states (amplitudes) instead of the explicit wavefunctions (amplitudes and phases), thus electron interference effects are not considered. Using the 3D-WKB method the N atom always shows up as a protrusion in the STM image as it is expected from the relation of the density of states of the N and C atoms [19].

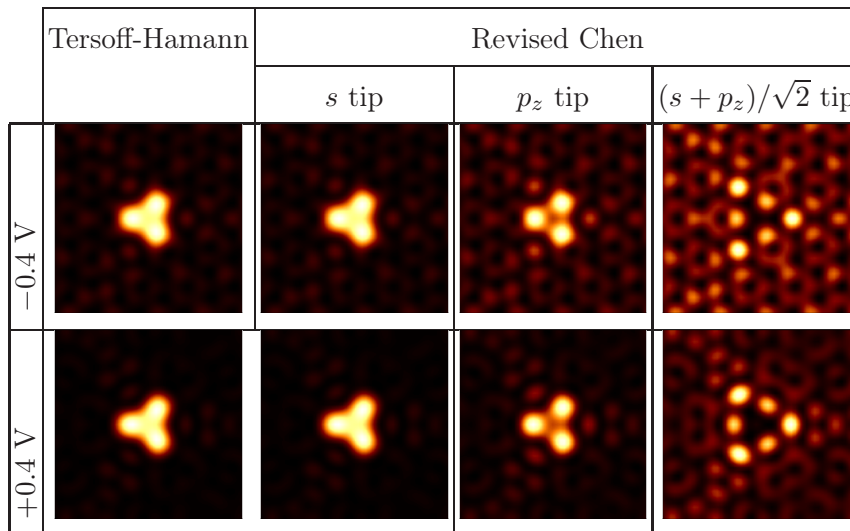


Figure 1. Constant height STM images of N-doped graphene at 4 Å tip-sample distance and  $\pm 0.4$  V bias. Comparison between Tersoff-Hamann model and revised Chen’s method with selected tip orbitals:  $s$ ,  $p_z$ ,  $(s + p_z)/\sqrt{2}$ . The N defect is located in the middle of the images.

Next, we focus on the comparison of the revised Chen’s method with two conventional STM simulation models: Tersoff-Hamann and Bardeen. Fig. 1 shows that the STM images obtained by the revised Chen’s method using a pure  $s$  tip quantitatively agree with those calculated by the Tersoff-Hamann model, i.e., a correlation value of 1 between the corresponding STM images is found. We obtain qualitatively similar STM images assuming an ideal tip of pure  $p_z$  orbital, where the current dip above the N atom is slightly more pronounced than

with the  $s$  tip. For these tip models the energy independent weighting factors in section IIB (i) were used. Furthermore, we point out the importance of quantum interference of tip orbitals in Fig. 1. Therefore, we consider an ideal tip of a linear combination of  $s$  and  $p_z$  orbitals of equal weights. As can be seen, the  $(s + p_z)/\sqrt{2}$  tip shows a remarkable contrast change compared to the STM images of pure  $s$  or pure  $p_z$  orbitals, where the current dip above the N atom is even more pronounced and the bright triangle showing C atoms is larger and reversed. This effect is clearly related to the orbital interference of the tip's  $s$  and  $p_z$  states, and shows an additional effect to the destructive quantum interference arising from the sample's C-N bond in the formation of the STM contrast of N-doped graphene. We stress again that the  $s - p_z$  tip orbital interference results in a much more pronounced current dip above the N atom than the destructive quantum interference of the sample itself, the latter is imaged by the Tersoff-Hamann method. Interestingly, STM images obtained by the  $(s + p_z)/\sqrt{2}$  tip resemble results calculated by a C(111) tip model (see Ref. [19]) having these dominant orbitals in the electronic structure. Note that both types of STM contrast of N-doped graphene in Fig. 1 have been experimentally observed in Ref. [19].

Fig. 2 and Table III show qualitative and quantitative comparisons of the revised Chen's method with Bardeen's method using three different tungsten tip models, which have also been used in previous studies of STM imaging of HOPG [10, 25]. Moreover, we compare two different choices of the  $C_{\nu\beta}$  weighting coefficients in Eq. (6) of the revised Chen's method, see section IIB (ii) and (iii), and good qualitative agreement is obtained.

We find that using these methods the current dip above the N atom is always present in the STM images in Fig. 2. The degree of agreement between Bardeen's and revised Chen's method, reported as correlation coefficients between corresponding STM images in Table III, depends on the actual tip geometry and electronic structure, hence the bias voltage. Let us recall that we expand the tip wavefunctions/density of states around the tip apex atom and calculate the  $C_{\nu\beta}$  coefficients in the Wigner-Seitz sphere of the tip apex atom in the revised Chen's method. The accuracy of such an expansion depends strongly on the neighboring sub-apex atoms' electronic structure and on the tip-sample distance. For example, for sharp tips the contribution of sub-apex atoms to the tunneling current is more important than for blunt tips [25]. On the other hand, the larger the tip-sample distance the better the agreement of STM images between the two methods. The reason is that with increasing tip-sample

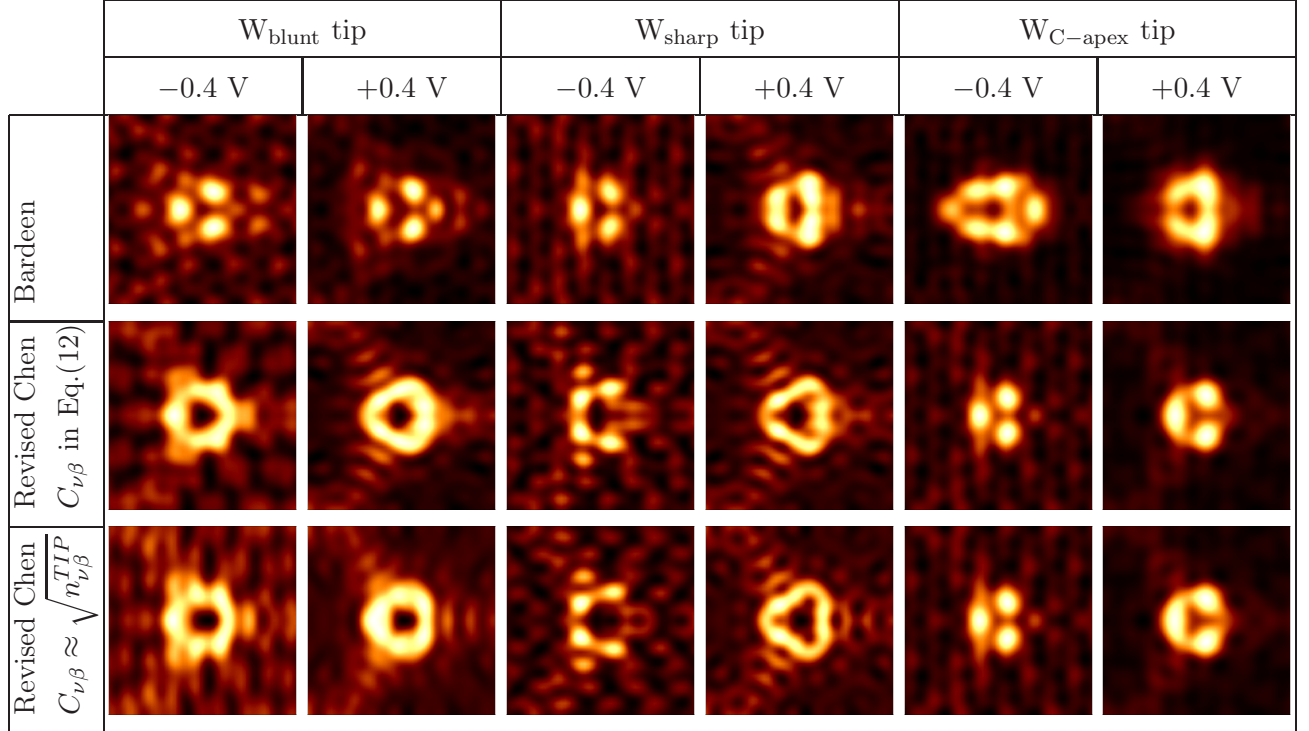


Figure 2. Constant height STM images of N-doped graphene at 4 Å tip-sample distance and  $\pm 0.4$  V bias. Comparison between Bardeen’s model and revised Chen’s method with two different choices of the  $C_{\nu\beta}$  weighting coefficients in Eq. (6) (see section II B (ii) and (iii) for details) for three tungsten tip models:  $W_{\text{blunt}}$ ,  $W_{\text{sharp}}$  and  $W_{\text{C-apex}}$ . Room temperature was assumed corresponding to the STM experiments in Ref. [19]. The N defect is located in the middle of the images.

separation the effect of the local tip geometry decreases. At larger tip-sample distances we find that the current dip above the N atom vanishes and a rounded triangular pattern is obtained leaving the three nearest neighbor C atoms visible, similarly to the Tersoff-Hamann results in Fig. 1.

Correlation coefficients between STM images in Fig. 2	$W_{\text{blunt}} \text{ tip}$		$W_{\text{sharp}} \text{ tip}$		$W_{\text{C-apex}} \text{ tip}$	
	-0.4 V	+0.4 V	-0.4 V	+0.4 V	-0.4 V	+0.4 V
Bardeen-Revised Chen ( $C_{\nu\beta}$ in Eq.(12))	0.81	0.82	0.78	0.89	0.73	0.91
Bardeen-Revised Chen ( $C_{\nu\beta} \approx \sqrt{n_{\nu\beta}^{TIP}}$ )	0.71	0.81	0.62	0.79	0.74	0.92

Table III. Quantitative comparison between Bardeen’s model and revised Chen’s method: calculated correlation coefficients between STM images in Fig. 2.



Overall, we find good agreement between Bardeen’s and revised Chen’s method in Fig. 2 and Table III. Calculated correlation values are above 0.7 except for the  $W_{\text{sharp}}$  tip at  $-0.4$  V bias and  $C_{\nu\beta} \approx \sqrt{n_{\nu\beta}^{\text{TIP}}}$ . We find better correlation for  $C_{\nu\beta}$  in Eq.(12) than for the  $C_{\nu\beta} \approx \sqrt{n_{\nu\beta}^{\text{TIP}}}$  approximation used in the revised Chen’s method, with the exception of the  $W_{\text{C-apex}}$  tip. Moreover, systematically better correlation between Bardeen’s and revised Chen’s method is found for  $+0.4$  V than for  $-0.4$  V bias voltage. Note that the large difference between STM images of the  $W_{\text{sharp}}$  tip with different bias polarities can be explained by the asymmetric electronic structure of the tip apex around the Fermi level [10, 25].

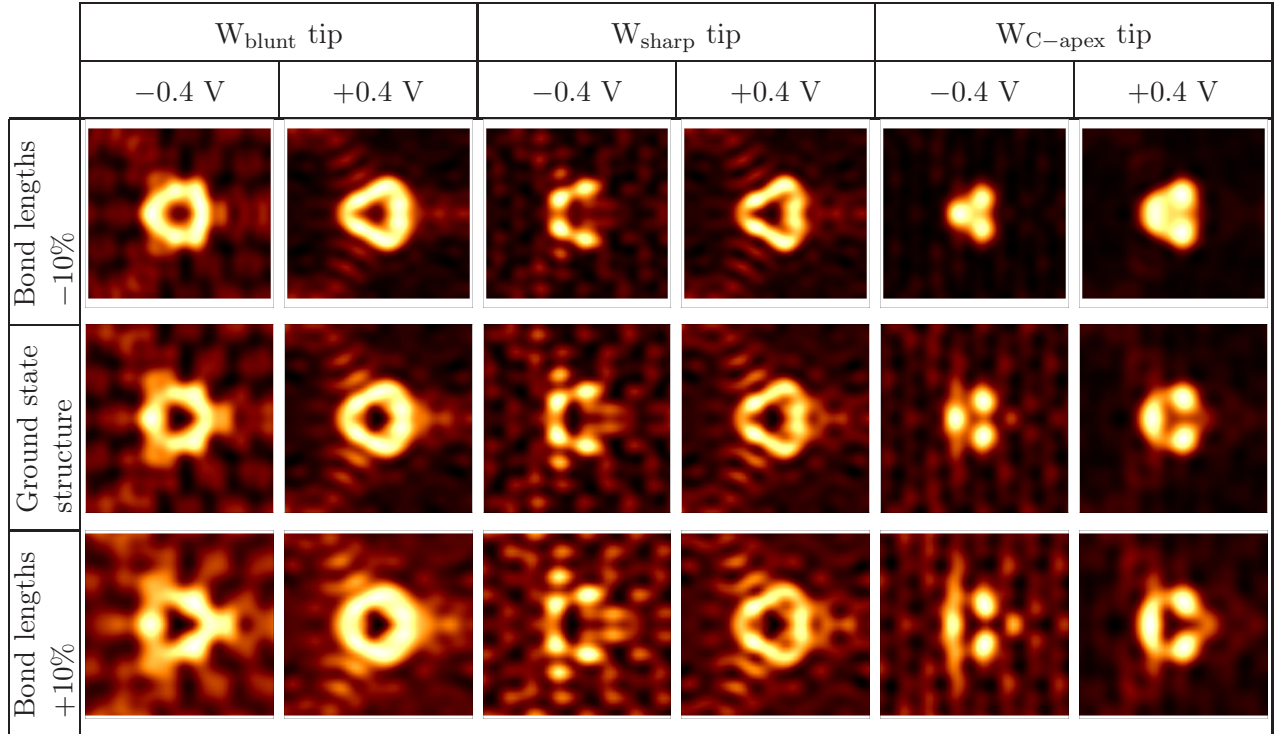


Figure 3. Effect of strain on constant height STM images of N-doped graphene at  $4 \text{ \AA}$  tip-sample distance and  $\pm 0.4$  V bias using the revised Chen’s method with three tungsten tip models:  $W_{\text{blunt}}$ ,  $W_{\text{sharp}}$  and  $W_{\text{C-apex}}$ . The ground state N-doped graphene geometry obtained by DFT and two other structures with bond lengths varied by  $\pm 10\%$  relative to the ground state are compared.

It is interesting to investigate the effect of strain on the obtained STM contrast. Fig. 3 shows a comparison between STM images calculated for three different N-doped graphene geometries with varying bond lengths by  $\pm 10\%$  relative to the ground state structure, which has been obtained by DFT calculation with C-N and C-C bond lengths of  $1.42 \text{ \AA}$ . Generally, we observe that the main features of the STM contrast do not change with the applied strain.

This is quantitatively confirmed by correlation coefficients being above 0.93 for each tip and bias combination calculated between images within each column of Fig. 3. We find a tendency of spatially extended brighter features in the STM images upon elongation of the bonds.

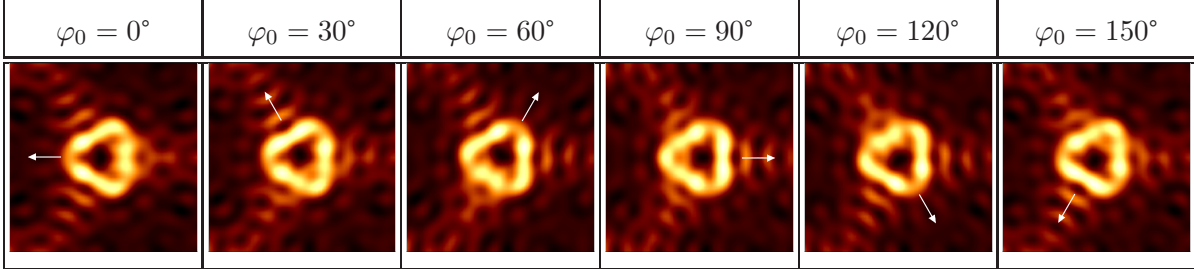


Figure 4. Tip rotation effect on the constant height STM images of N-doped graphene calculated with  $W_{\text{sharp}}$  tip at 4 Å tip-sample distance and +0.4 V bias voltage. The rotation axis of the tip is perpendicular to the surface ( $\vartheta_0 = \psi_0 = 0^\circ$ ). The orientations of the brightest features are indicated by white arrows in each STM image.

In the following we investigate the effect of tip rotations on the STM images. Constant height STM images have been calculated above the N-doped graphene surface with the tungsten tip models at 4 Å tip-sample distance. We considered tip rotations around the axis perpendicular to the sample surface. This corresponds to  $\vartheta_0 = 0^\circ$ , and in this case rotations with respect to  $\varphi_0$  and  $\psi_0$  are equivalent, thus, we fixed  $\psi_0 = 0^\circ$  and rotated the tip by  $\varphi_0$  in  $10^\circ$  steps. Since a more asymmetric tip is expected to have a larger tip rotational effect, we present results obtained by the  $W_{\text{sharp}}$  tip at +0.4 V bias voltage. Selected STM images are shown in Fig. 4.

Due to the  $C_{2v}$  symmetry of the tip, the same image is obtained for  $\varphi_0 = 180^\circ$  as for  $\varphi_0 = 0^\circ$ . We find that the current dip above the N atom is always present independently of the degree of tip rotation by  $\varphi_0$ , but the intensity of the current above the surrounding C atoms changes with the tip rotation. There are certain directions denoted by white arrows in Fig. 4, where the brightest features occur that correspond to the largest currents above or close to nearest neighbor C atoms. These indicated directions rotate twice faster than the tip rotation by  $\varphi_0$  itself. The finding that such kind of tip rotations, where the  $z$  axis of the tip is not tilted with respect to the  $z$  axis of the sample ( $\vartheta_0 = 0^\circ$ ), affect the secondary features of the STM image is in agreement with previous results using the 3D-WKB method [25, 26].

In Fig. 5 we extracted line sections of the constant height STM images presented in Fig.

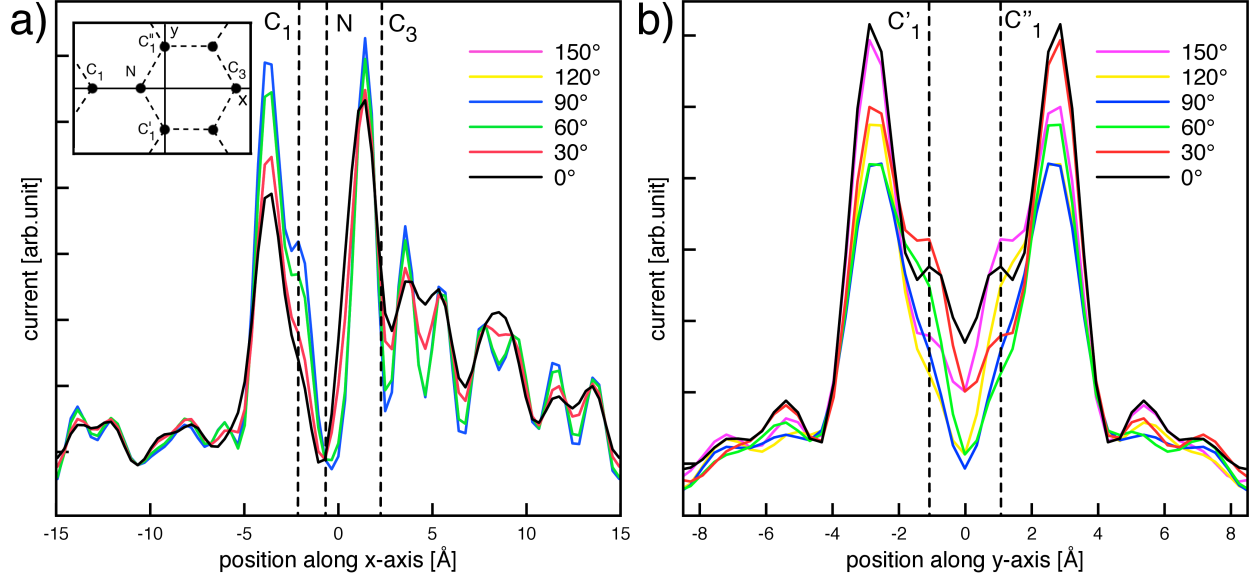


Figure 5. Current profiles along  $x$  and  $y$  directions of the N-doped graphene surface (see inset) as a function of tip rotation with respect to  $\varphi_0$ . ( $\vartheta_0 = \psi_0 = 0^\circ$ )

4. The line along the  $x$  direction contains the N atom and its nearest ( $C_1$ ) and third nearest neighbor ( $C_3$ ) carbon atoms. The line along the  $y$  direction contains the other two nearest neighbor carbon atoms ( $C'_1$  and  $C''_1$ ), see the inset of Fig. 5a). The symmetries of the sample and the tip are reflected in these line sections as well. We find indeed that the current value above the N atom is insensitive to the tip rotation, and it is almost the smallest current value in the entire scan area. We can also see that the brightest features, i.e., the largest current values of the STM images are actually not located above the carbon atoms, but rather above the hollow positions of the honeycomb lattice.

## B. $Mn_2H$ on Ag(111) surface

Sachse *et al.* found that  $Mn_2H$  on the Ag(111) surface can produce STM images with single or double features depending on the magnetic coupling between Mn atoms [22]. Double features have been obtained at positive bias employing the Tersoff-Hamann method for an antiferromagnetic Mn-Mn coupling, which corresponds to the energetically favored ground state. The calculated relaxed geometry of antiferromagnetic  $Mn_2H$  on the Ag(111) surface is

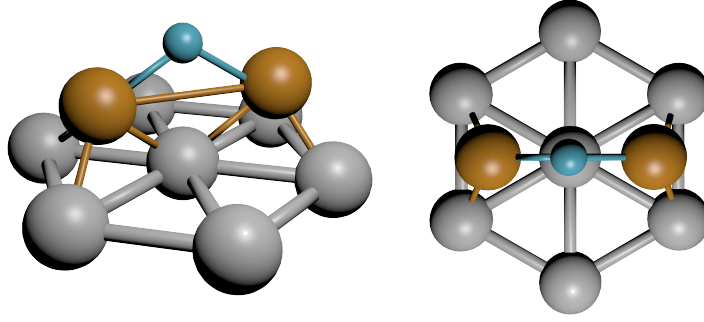


Figure 6. Calculated relaxed geometry of antiferromagnetic  $\text{Mn}_2\text{H}$  on the  $\text{Ag}(111)$  surface. Data is taken from Ref. [22].

shown in Fig. 6. We consider this system and perform an investigation of its STM imaging depending on three employed tunneling models: Bardeen, revised Chen and Tersoff-Hamann. Using the decomposition of the tunneling current according to Eq. (7) in the revised Chen’s method, we are able to identify the physical origin of the observed dip above  $\text{Mn}_2\text{H}$ .

The calculated constant height STM images at small bias voltages ( $\pm 0.1$  V) using two silver blunt tip models [ $\text{Ag}(001)$  and  $\text{Ag}(111)$ ] are shown in Fig. 7. Correlation coefficients between STM images obtained by Bardeen’s and revised Chen’s method are reported in Table IV. First of all, we find excellent quantitative agreement between the STM images obtained by Bardeen’s and revised Chen’s method for the  $\text{Ag}(111)$  tip and good agreement for the  $\text{Ag}(001)$  tip. Recalling that the revised Chen’s method is 25 times faster than Bardeen’s method in practical STM calculations, this clearly indicates that our proposed model is a very promising tool for STM simulations in the future. Moreover, the results in Fig. 7 show that the geometry and electronic structure of the tip have a considerable effect on the STM imaging of  $\text{Mn}_2\text{H}/\text{Ag}(111)$ :  $\text{Ag}(001)$  tip provides single protrusion and  $\text{Ag}(111)$  tip provides double features of the STM images at both bias polarities using both Bardeen’s and revised Chen’s methods. However, the Tersoff-Hamann model provides qualitative agreement with these at selected bias voltages only: At  $-0.1$  V a single protrusion is obtained, while at  $+0.1$  V a double feature is visible. The comparison of the Tersoff-Hamann results with those obtained by the revised Chen’s method suggests a contradiction with the general assumption of Ag tips being of  $s$  orbital character [22]. In order to understand the components of the tunneling current above the H atom, the decomposition according to Eq. (7) in the revised

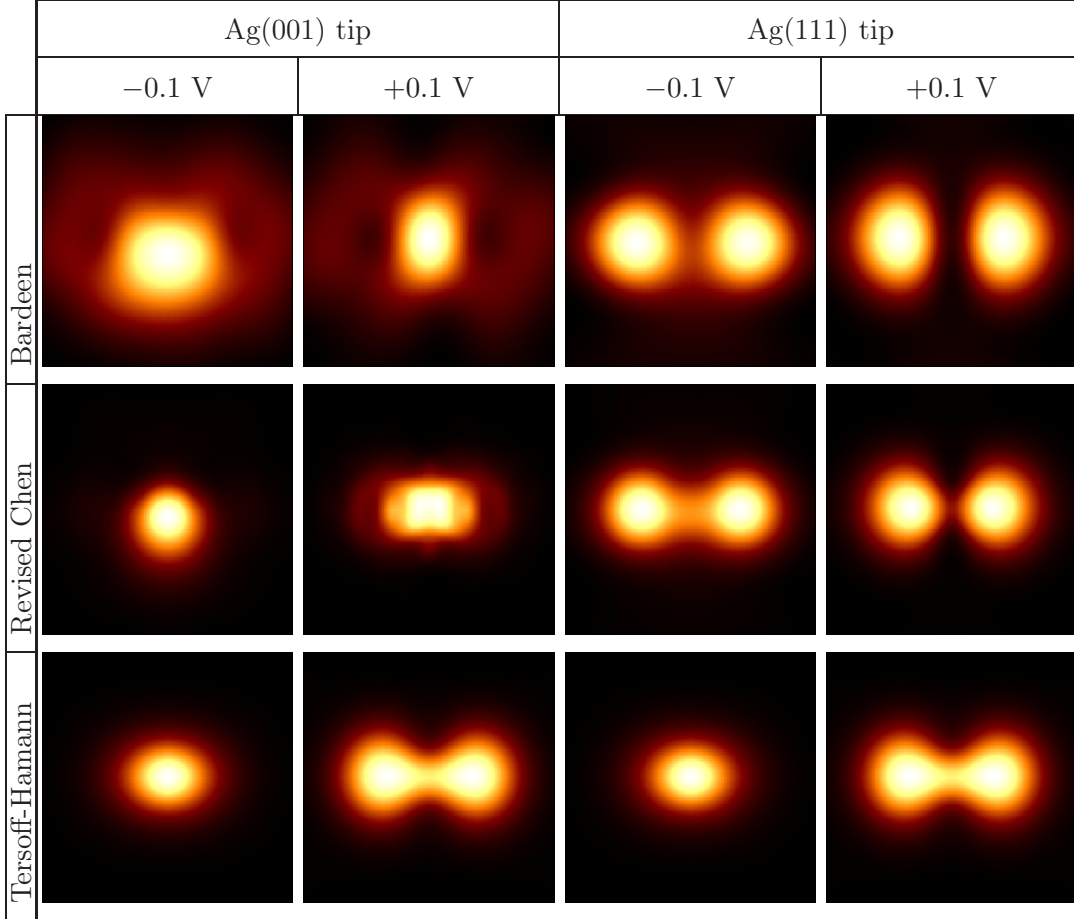


Figure 7. Constant height STM images of antiferromagnetic  $\text{Mn}_2\text{H}$  on the Ag(111) surface simulated at 5 Å Ag surface-tip distance and  $\pm 0.1$  V bias with three different methods (Bardeen, revised Chen, Tersoff-Hamann) and two blunt tip models: Ag(001) and Ag(111). A temperature of 7 K was assumed corresponding to the STM experiments in Ref. [22]. Note that results of the Tersoff-Hamann model are shown for comparison reasons only, and no explicit tip electronic structure is considered there.

Chen’s method is employed.

Fig. 8 shows the results of the current decomposition according to tip orbital characters. Interestingly, we find that the Ag(001) tip does not behave as an  $s$ -type tip at +0.1 V bias [see Fig. 8a)]. The major contributions are from the  $p_x$ ,  $p_y$ ,  $d_{xz}$  and  $d_{yz}$  tip orbitals, and there are destructive interferences arising from  $p_x - d_{xz}$  and  $p_y - d_{yz}$  tip orbitals. This explains the qualitative disagreement between the Tersoff-Hamann and revised Chen’s results for the Ag(001) tip at +0.1 V bias. On the other hand, using the Ag(111) tip at  $-0.1$  V bias,

Correlation coefficients between STM images in Fig. 7	Ag(001) tip		Ag(111) tip	
	-0.1 V	+0.1 V	-0.1 V	+0.1 V
Bardeen-Revised Chen ( $C_{\nu\beta}$ in Eq.(12))	0.72	0.88	0.97	0.95

Table IV. Quantitative comparison between Bardeen’s model and revised Chen’s method: calculated correlation coefficients between STM images in Fig. 7.

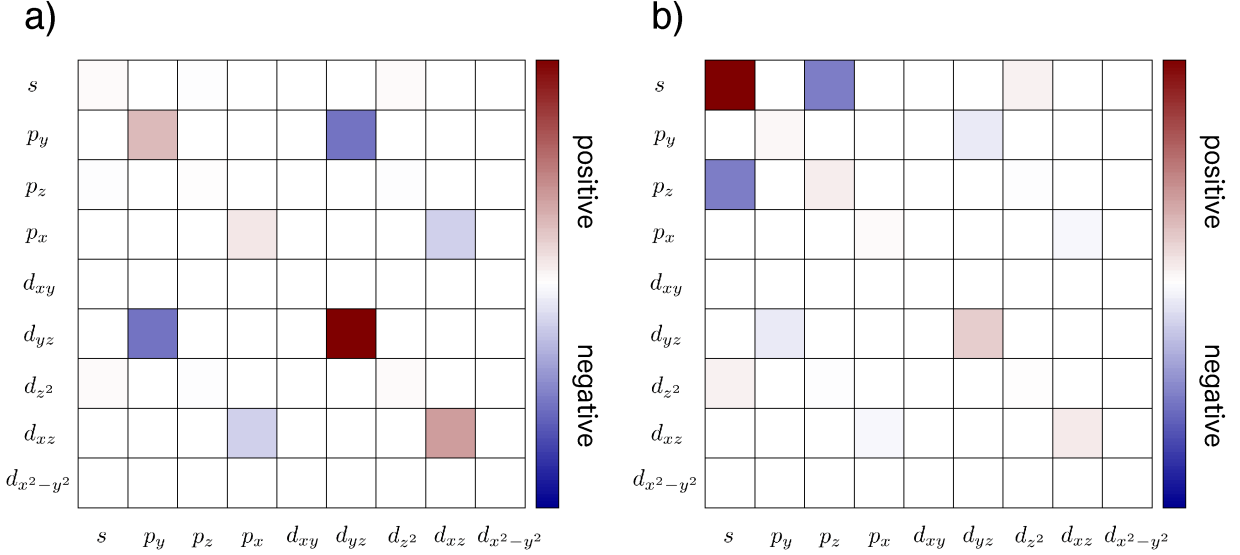


Figure 8. Decomposition of the tunneling current  $1.83 \text{ \AA}$  above the H atom in  $\text{Mn}_2\text{H}/\text{Ag}(111)$  (corresponding to Fig. 7) using Eq. (7). Diagonal: direct (positive) contributions, off-diagonal: interference (positive or negative) contributions to the current. a) Ag(001) tip at bias voltage  $V = +0.1 \text{ V}$ , b) Ag(111) tip at bias voltage  $V = -0.1 \text{ V}$ .

the major contribution is clearly from the tip’s  $s$  orbital [see Fig. 8b)]. Apart from that there is a strong  $s - p_z$  destructive tip interference that is missing in the Tersoff-Hamann model, causing the observed qualitative difference in the STM images for the Ag(111) tip at  $-0.1 \text{ V}$  bias. Moreover, we find similar current decomposition characteristics for the Ag(001) tip at  $-0.1 \text{ V}$  bias and for the Ag(111) tip at  $+0.1 \text{ V}$  bias as Fig. 8b) shows, with a dominating  $s$  orbital contribution from the tip. For these tip and bias voltage combinations a good qualitative agreement of the STM images between revised Chen’s and Tersoff-Hamann results is obtained. Our findings suggest that although the quality of the STM contrast

(single or double feature) is mainly determined by the electronic states of the sample surface that can be captured by employing the Tersoff-Hamann model, the tip electronic structure and in the present case an  $s - p_z$  destructive tip interference can cause a contrast change.

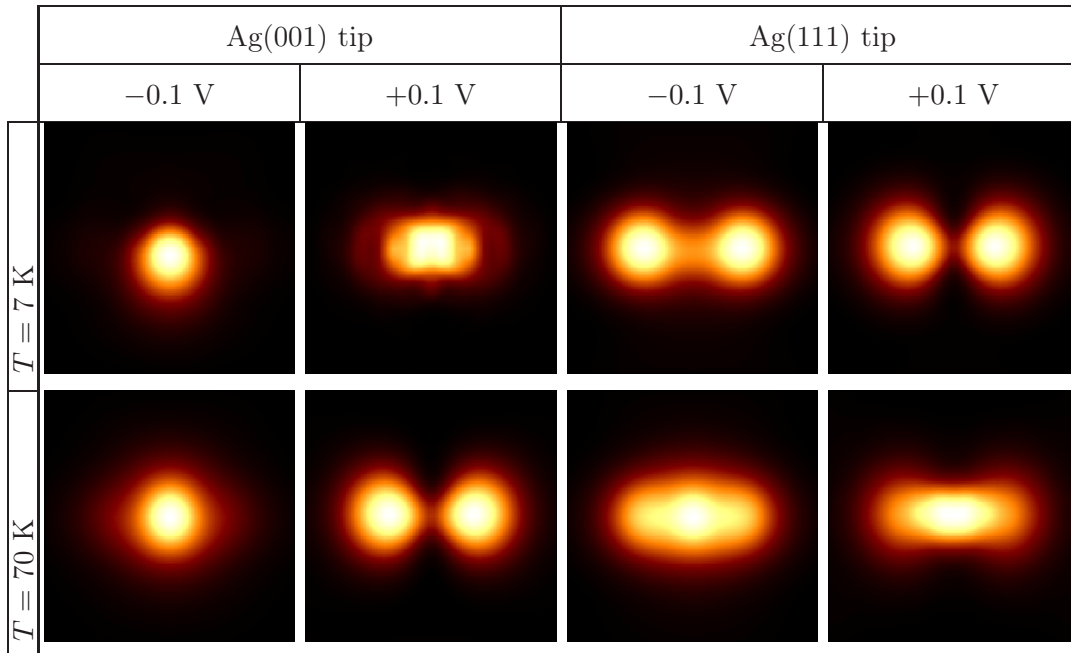


Figure 9. Effect of temperature on constant height STM images of antiferromagnetic  $\text{Mn}_2\text{H}$  on the Ag(111) surface simulated at  $5 \text{ \AA}$  Ag surface-tip distance and  $\pm 0.1 \text{ V}$  bias using the revised Chen’s method with two blunt tip models: Ag(001) and Ag(111). Temperatures of  $T = 7 \text{ K}$  and  $70 \text{ K}$  are compared.

It is important to highlight the effect of temperature on the obtained STM contrast. Temperature enters into the tunneling model exactly in the same fashion as in the well established Bardeen’s model, i.e., in two ways: (i) the thermal broadening of the electron states, see Eq.(3), and (ii) the energy window for calculating the tunneling channels, where nonzero temperature results in an extension of the energy window due to the Fermi distribution, see Eq.(1). Fig. 9 shows a comparison between STM images calculated at  $T = 7 \text{ K}$  and  $70 \text{ K}$ , the former corresponding to the temperature used in the experiments of Ref. [22]. We find a diverse behavior of the STM contrast at the higher temperature depending on the tip and bias voltage. The contrast (single protrusion) is preserved for the Ag(001) tip at  $-0.1 \text{ V}$  only. The other three images show different contrasts at the two temperatures. Upon increasing the temperature, for the Ag(001) tip at  $+0.1 \text{ V}$  the single protrusion contrast changes to

double features, while for the Ag(111) tip at both bias voltages the double protrusion contrast changes to an elongated single feature with the maximal current above the H atom of Mn<sub>2</sub>H. This diversity of simulated STM contrasts points to the importance of the correct choice of temperature in STM simulations if a meaningful explanation of given experimental STM data is desired.

## V. CONCLUSIONS

We revised Chen's derivative rule for electron tunneling for the purpose of computationally efficient STM simulations based on first principles electronic structure data. The revised Chen's model includes the electronic structure and arbitrary spatial orientation of the tip by taking appropriate weighting coefficients of tunneling matrix elements of different tip orbital characters. Interference of tip orbitals in the STM junction is included in the model by construction. We demonstrated the reliability of the model by applying it to two functionalized surfaces of recent interest where quantum interference effects play an important role in the STM imaging process: N-doped graphene and an antiferromagnetic Mn<sub>2</sub>H complex on the Ag(111) surface. We found that the revised Chen's model is 25 times faster than the Bardeen method concerning computational time, while maintaining good agreement. Our results show that the electronic structure of the tip has a considerable effect on STM images, and the Tersoff-Hamann model does not always provide sufficient results in view of quantum interference effects. For both studied surfaces we highlighted the importance of interference between  $s$  and  $p_z$  tip orbitals that can cause a significant contrast change in the STM images. Moreover, our findings show that stretched bonds have a minor effect on the main features of the STM contrast, and temperature is an important factor to be taken into account in STM simulations if aiming at accuracy in comparison with experiments. Our method implemented in the BSKAN code, thus, provides a fast and reliable tool for calculating STM images based on Chen's derivative rule taking into account the electronic structure and local geometry of the tip apex.



## ACKNOWLEDGMENTS

The authors thank P. Mutombo and P. Jelínek for insightful discussions concerning N-doped graphene and T. Sachse and W. A. Hofer for useful discussions and electronic structure data of Mn<sub>2</sub>H/Ag(111). Financial support of the Hungarian State Eötvös Fellowship, Hungarian Scientific Research Fund project OTKA PD83353, the Bolyai Research Grant of the Hungarian Academy of Sciences, and the New Széchenyi Plan of Hungary (Project ID: TÁMOP-4.2.2.B-10/1-2010-0009) is gratefully acknowledged. Usage of the computing facilities of the Wigner Research Centre for Physics and the BME HPC Cluster is kindly acknowledged.

- 
- [1] J. Bardeen. Tunnelling from a many-particle point of view. *Phys. Rev. Lett.* 6, 57–9 (1961).
  - [2] K. Palotás and W. A. Hofer. Multiple scattering in a vacuum barrier obtained from real-space wavefunctions. *J. Phys.: Condens. Matter* 17, 2705–13 (2005).
  - [3] W. A. Hofer. Challenges and errors: interpreting high resolution images in scanning tunneling microscopy. *Prog. Surf. Sci.* 71, 147–83 (2003).
  - [4] N. Mingo, L. Jurczyszyn, F. J. Garcia-Vidal, R. Saiz-Pardo, P. L. De Andres, F. Flores, S. Y. Wu, and W. More. Theory of the scanning tunneling microscope: Xe on Ni and Al. *Phys. Rev. B* 54, 2225–35 (1996).
  - [5] J. Tersoff and D. R. Hamann. Theory and application for the scanning tunneling microscope. *Phys. Rev. Lett.* 50, 1998–2001 (1983).
  - [6] J. Tersoff and D. R. Hamann. Theory of the scanning tunneling microscope. *Phys. Rev. B* 31, 805–13 (1985).
  - [7] C. J. Chen. Tunneling matrix elements in three-dimensional space: The derivative rule and the sum rule. *Phys. Rev. B* 42, 8841–57 (1990).
  - [8] K. Palotás, G. Mándi, and W. A. Hofer. Three-dimensional Wentzel-Kramers-Brillouin approach for the simulation of scanning tunneling microscopy and spectroscopy. *Front. Phys.* 9, 711–47 (2014).
  - [9] K. Palotás, G. Mándi, and L. Szunyogh. Orbital-dependent electron tunneling within the atom superposition approach: Theory and application to W(110). *Phys. Rev. B* 86, 235415 (2012).

- [10] G. Teobaldi, E. Inami, J. Kanasaki, K. Tanimura, and A. L. Shluger. Role of applied bias and tip electronic structure in the scanning tunneling microscopy imaging of highly oriented pyrolytic graphite. *Phys. Rev. B* 85, 085433 (2012).
- [11] A. N. Chaika, S. S. Nazin, V. N. Semenov, S. I. Bozhko, O. Lübben, S. A. Krasnikov, K. Radican, and I. V. Shvets. Selecting the tip electron orbital for scanning tunneling microscopy imaging with sub-ångström lateral resolution. *EPL* 92, 46003 (2010).
- [12] A. N. Chaika, S. S. Nazin, V. N. Semenov, N. N. Orlova, S. I. Bozhko, O. Lübben, S. A. Krasnikov, K. Radican, and I. V. Shvets. High resolution STM imaging with oriented single crystalline tips. *Appl. Surf. Sci.* 267, 219–23 (2013).
- [13] H. S. Wong, X. Feng, K. Müllen, N. Chandrasekhar, and C. Durkan. Channel selective tunnelling through a nanographene assembly. *Nanotechnology* 23, 095601 (2012).
- [14] L. Gross, N. Moll, F. Mohn, A. Curioni, G. Meyer, F. Hanke, and M. Persson. High-resolution molecular orbital imaging using a p-wave STM tip. *Phys. Rev. Lett.* 107, 086101 (2011).
- [15] B. Siegert, A. Donarini, and M. Grifoni. The role of the tip symmetry on the STM topography of  $\pi$ -conjugated molecules. *Phys. Stat. Sol. B* 250, 2444–51 (2013).
- [16] G. Mándi and K. Palotás. STM contrast inversion of the Fe(110) surface. *Appl. Surf. Sci.* 304, 65–72 (2014).
- [17] I. Suominen, J. Nieminen, R. S. Markiewicz, and A. Bansil. Effect of orbital symmetry of the tip on scanning tunneling spectra of  $\text{Bi}_2\text{Sr}_2\text{CaCu}_2\text{O}_{8+\delta}$ . *Phys. Rev. B* 84, 014528 (2011).
- [18] E. H. da Silva Neto, P. Aynajian, R. E. Baumbach, E. D. Bauer, J. Mydosh, S. Ono, and A. Yazdani. Detection of electronic nematicity using scanning tunneling microscopy. *Phys. Rev. B* 87, 161117 (2013).
- [19] M. Telychko, P. Mutombo, M. Ondráček, P. Hapala, F. C. Bocquet, J. Kolorenč, M. Vondráček, P. Jelínek, and M. Švec. Achieving high-quality single-atom nitrogen doping of Graphene/SiC(0001) by ion implantation and subsequent thermal stabilization. *ACS Nano* 8, 7318–24 (2014).
- [20] L. Jurczyszyn and B. Stankiewicz. Inter-orbital interference in STM tip during electron tunneling in tip–sample system: influence on STM images. *Prog. Surf. Sci.* 74, 185–200 (2003).
- [21] L. Jurczyszyn and B. Stankiewicz. The role of interorbital interference in the formation of STS spectra. *Appl. Surf. Sci.* 242, 70–81 (2005).

- [22] T. Sachse, N. Néel, S. Meierott, R. Berndt, W. A. Hofer, and J. Kröger. Electronic and magnetic states of  $\text{Mn}_2$  and  $\text{Mn}_2\text{H}$  on  $\text{Ag}(111)$ . *New J. Phys.* 16, 063021 (2014).
- [23] J. H. A. Hagelaar, C. F. J. Flipse, and J. I. Cerdá. Modeling realistic tip structures: Scanning tunneling microscopy of NO adsorption on  $\text{Rh}(111)$ . *Phys. Rev. B* 78, 161405 (2008).
- [24] A. J. Lakin, C. Chiutu, A. M. Sweetman, P. Moriarty, and J. L. Dunn. Recovering molecular orientation from convoluted orbitals. *Phys. Rev. B* 88, 035447 (2013).
- [25] G. Mándi, G. Teobaldi, and K. Palotás. Contrast stability and 'stripe' formation in scanning tunneling microscopy imaging of highly oriented pyrolytic graphite: the role of STM-tip orientations. *J. Phys.: Condens. Matter* 26, 485007 (2014).
- [26] G. Mándi, N. Nagy, and K. Palotás. Arbitrary tip orientation in STM simulations: 3D-WKB theory and application to  $\text{W}(110)$ . *J. Phys.: Condens. Matter* 25, 445009 (2013).
- [27] G. Mándi, G. Teobaldi, and K. Palotás. What is the orientation of the tip in a scanning tunneling microscope? *Prog. Surf. Sci.* 90, 223–38 (2015).
- [28] G. Kresse and J. Furthmüller. Efficient iterative schemes for ab initio total-energy calculations using a plane-wave basis set. *Phys. Rev. B* 54, 11169–86 (1996).
- [29] X. Gonze et al. ABINIT: First-principles approach of materials and nanosystem properties. *Computer Phys. Commun.* 180, 2582–2615 (2009).
- [30] P. Giannozzi et al. QUANTUM ESPRESSO: a modular and open-source software project for quantum simulations of materials. *J. Phys.: Condens. Matter* 21, 395502 (2009).
- [31] G. Kresse and D. Joubert. From ultrasoft pseudopotentials to the projector augmented-wave method. *Phys. Rev. B* 59, 1758–75 (1999).
- [32] J. P. Perdew and Y. Wang. Accurate and simple analytic representation of the electron-gas correlation energy. *Phys. Rev. B* 45, 13244–49 (1992).
- [33] H. J. Monkhorst and J. D. Pack. Special points for Brillouin-zone integrations. *Phys. Rev. B* 13, 5188–92 (1976).
- [34] J. P. Perdew, K. Burke, and M. Ernzerhof. Generalized gradient approximation made simple. *Phys. Rev. Lett.* 77, 3865–8 (1996).